

## Hybridized propagating spin waves in a CoFeB/IrMn bilayer

Hanchen Wang<sup>1,2,\*</sup>, Wenqing He<sup>3,\*</sup>, Rundong Yuan<sup>1,\*</sup>, Yizhan Wang<sup>3,\*</sup>, Jinlong Wang<sup>1,\*</sup>, Yu Zhang<sup>3</sup>,  
Israa Medlej<sup>4,2</sup>, Jilei Chen<sup>4</sup>, Guoqiang Yu<sup>3</sup>, Xiufeng Han<sup>3,†</sup>, Jean-Philippe Ansermet<sup>5,2,‡</sup> and Haiming Yu<sup>1,2,§</sup>

<sup>1</sup>Fert Beijing Institute, MIIT Key Laboratory of Spintronics, School of Integrated Circuit Science and Engineering, Beihang University, Beijing 100191, China

<sup>2</sup>International Quantum Academy, Shenzhen 518055, China

<sup>3</sup>Beijing National Laboratory for Condensed Matter Physics, Institute of Physics, University of Chinese Academy of Sciences, Chinese Academy of Sciences, Beijing 100190, China

<sup>4</sup>Shenzhen Institute for Quantum Science and Engineering (SIQSE), and Department of Physics, Southern University of Science and Technology (SUSTech), Shenzhen 518055, China

<sup>5</sup>Institute of Physics, École Polytechnique Fédérale de Lausanne (EPFL), 1015, Lausanne, Switzerland



(Received 27 April 2022; revised 3 July 2022; accepted 28 July 2022; published 5 August 2022)

In this work, we report the propagating spin waves hybridized between first-order and quasiuniform modes in a  $\text{Co}_{20}\text{Fe}_{60}\text{B}_{20}$  thin film capped by  $\text{Ir}_{25}\text{Mn}_{75}$ . The anticrossing gaps are observed at room temperature both in the reflection and transmission spectra, where the coupling strength can be tuned by varying the value of the in-plane wave vector at which the dispersion curves cross. The key mechanism behind this feature is theoretically ascribed to the dipole-dipole interaction by a model which accounts for many features of our experimental results. The strong coupling with a cooperativity up to 2.0 is achieved with taking the dissipation rates of two coupled branches into account. A reference CoFeB sample without IrMn reveals that the interfacial pinning effect also plays a role in the magnon-magnon hybridization. Tunable hybridization of magnons may foster the field of magnonics in information processing.

DOI: [10.1103/PhysRevB.106.064410](https://doi.org/10.1103/PhysRevB.106.064410)

### I. INTRODUCTION

Control over the coherent coupling between quasiparticles is a key issue in realizing information manipulation in quantum technology [1–5]. Magnons, the quasiparticle of spin waves, are the low-energy collective excitations of magnetic moments with long-range order [6–15]. The coupling between electrodynamics and magnons has attracted extensive attention [16–18], and lots of hybridized magnon modes have been experimentally observed, such as magnon polaritons [19–28], magnon polarons [29–34], magnon-superconductor qubits [4,35,36], and magnon excitons [37]. In addition, the hybridization between multiple magnon modes in antiferromagnets and ferrimagnets provides a platform for a coherent control and engineer spin dynamics, of which the coupling strength can be tuned via interlayer dipolar or interfacial exchange interactions in heterostructure systems [38–45]. However, detailed experimental investigations for coherent control of the coupling strength of hybridized propagating spin waves are still rare within single layer material. In addition, the coupling between standing spin waves and magnetostatic spin waves (MSSW) is widely available in different magnetic systems. When perpendicular standing spin waves

(PSSW) are hybridized with propagating MSSW mode, the PSSW can propagate in the film plane [46–49] and heterosymmetric spin waves (PSSW mode with in-plane wave vector) are coherently generated, as shown recently by time-resolved x-ray microscopy [47].

In this paper, we report the tunable magnon-magnon coupling between heterosymmetric (first-order mode,  $n = 1$ ) and in-plane propagating dipole-exchange spin waves (quasiuniform mode,  $n = 0$ ) in an  $\text{Ir}_{25}\text{Mn}_{75} / \text{Co}_{20}\text{Fe}_{60}\text{B}_{20}$  bilayer at room temperature. From the ferromagnetic resonance (FMR) spectra, the frequencies of FMR and PSSW modes are separated from one another. However, the nanostripline (NSL) antennas can excite in-plane spin waves with a broad wave vector distribution. The dispersion of the exchange-dominated first-order mode is relatively flat compared with that of the quasiuniform mode, and therefore they can cross with each other. The wave vector of the crossing point is included in the broad wave vector distribution of the NSL antennas. As a consequence, an anticrossing gap is observed both in the reflection and transmission spectra corresponding to the hybridized propagating spin waves. In addition, by applying different field strengths and directions with respect to antenna, the coupling strength  $g$  can be tuned and presents a linear relationship with respect to the crossing wave vector values  $k_c$ . Theory shows that this coupling feature is due to the off-diagonal parts of the dipolar interaction tensor. In addition, with the help of phenomenological loss theory [7], the effective dissipation rates of two coupled branches are calculated based on the intrinsic linewidths estimated from FMR spectra,

\*These authors contributed equally to this work.

†xfhan@iphy.ac.cn

‡jean-philippe.ansermet@epfl.ch

§haiming.yu@buaa.edu.cn

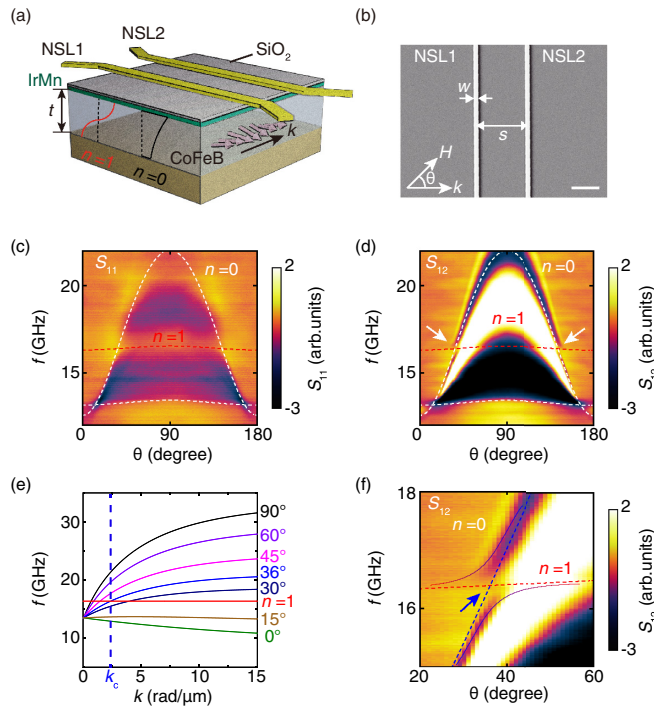


FIG. 1. (a) Illustrative diagram of the device structure. The measured sample is composed of a CoFeB layer with thickness  $t$  of 80 nm and an IrMn layer with SiO<sub>2</sub> capping on the top to prevent oxidation. (b) The scanning electron microscope (SEM) image of the NSL antennas, where the scale bar is 1  $\mu\text{m}$  and the angle between the external magnetic field and wave vector direction is defined as  $\theta$ . (c),(d) Angle-dependent reflection (dBmag) and transmission (Imag) spectra measured by NSL antennas, where the red and white dashed lines are the theoretical fittings of the first-order and quasiuniform modes by Eqs. (2) and (4), respectively. The white arrows point to the observed anticrossing gaps at  $90 \pm 54^\circ$ . (e) Theoretically calculated dispersions of first-order and quasiuniform modes at different angle  $\theta$ . The blue dashed line implies the crossing wave vector between first-order and quasiuniform modes at  $36^\circ$ . (f) The zoom-in transmission spectra at the anticrossing gap, where the blue dashed line is the theoretical fitting of the quasiuniform mode with wave vector of 2.5 rad/ $\mu\text{m}$  and the red dashed line is for the first-order mode. The two solid curves indicate the hybridized propagating modes.

which is further used to calculate accurately the cooperativity of the magnon-magnon coupling. The coupling can reach the strong coupling regime under large fields with a cooperativity up to 2.0 at 200 mT. Comparative measurements show that the existence of the IrMn layer can promote the coupling between first-order and quasiuniform modes owing to the interfacial pinning effect [48,50–52].

## II. SAMPLE AND EXPERIMENT

The CoFeB/IrMn heterostructures are grown on SiO<sub>x</sub> substrate by a magnetron sputtering system (ULVAC) at room temperature, where the thickness  $t$  of CoFeB [Fig. 1(a)] is fixed at 80 nm. During the growth process, the chamber base pressure is lower than  $3 \times 10^{-6}$  Pa, and an in-plane external magnetic field of 180 Oe is applied to induce the

exchange bias (pinning) between the CoFeB/IrMn interface. Subsequently, 10-nm-thick SiO<sub>2</sub> is deposited on the whole sample to prevent the oxidation. We first use optical lithography to pattern the photoresist on the sample into several parallelogram-shaped spin wave waveguides of which the edge is  $45^\circ$  to avoid spin-wave reflections, and then the ion beam etching is used to remove the materials without protecting the resist. With the help of electron beam lithography (EBL), two identical NSL antennas, which are made of Ti (10 nm)/Au (100 nm) by e-beam evaporation and lift-off process, are fabricated on top of spin-wave waveguides with different separated distances  $s$ .

As for the spin-wave measurements, we utilize the all-electric spin-wave spectroscopy (AESWS) with angle-resolved function, using a vector network analyzer (VNA) (Rohde and Schwarz ZVA 40) with frequency range up to 40 GHz. Two microwave cables are used to connect between the two ports from VNA and two microwave probes, which will further physically contact with the electrodes of NSL antennas and inject the rf current into them. Correspondingly, a dynamic electromagnetic field is generated to excite spin waves underneath the antenna and detect spin waves via the inverse physical process. The applied power for all experiments presented in this work is  $-10$  dBm and the IF bandwidth is 1 kHz. As shown in Fig. 1(a), two NSL antennas on the top of CoFeB with 80 nm thickness pinned by IrMn will not only excite the quasiuniform mode with the in-plane wave vector but also the first-order mode. The antennas are separated by a distance  $s$  of 2  $\mu\text{m}$  and the width of each antenna is 200 nm [see the SEM image in Fig. 1(b)]. The wave vector  $k_{\parallel}$  distribution of the 200-nm-wide NSL antenna is calculated by the fast Fourier transformation (FFT), which shows a broadband distribution starting from uniform precession (see Appendix A). We use a vibrating sample magnetometer (VSM) measurement to characterize the magnetic hysteresis loop along its pinning direction (easy axis) with in-plane magnetic fields, from which we can observe a clear squared hysteresis loop with about 1 mT exchange bias induced by the IrMn layer (see Appendix A). All the experiments are performed at room temperature. In addition, before all the spin-wave propagation measurements in this work, a large external magnetic field with strength of 300 mT is applied to saturate the whole sample. A reference spectrum is recorded at this large field which will be subtracted from the spectra recorded at other working fields to correct the background.

## III. RESULTS AND DISCUSSION

Before performing the propagating spin-wave measurements, we first use the flipchip measurement, where a submillimeter size coplanar waveguide (CPW) antenna is used to excite and detect the resonance of the whole chip to characterize the field- and angle-dependent FMR features of the sample. Two salient modes are observed: one is the FMR of CoFeB with stronger intensity but lower frequency and the other one is the PSSW mode with lower intensity but higher frequency (see Appendix B). Based on the field-dependent FMR spectra, we estimate the damping parameter of the film

by using the following equation [53]:

$$\delta f = \frac{|\gamma|}{2\pi} \mu_0 \Delta H + \frac{2}{\sqrt{3}} \alpha f, \quad (1)$$

where  $|\gamma| = 2\pi \times 28$  GHz/T is the gyromagnetic ratio,  $\Delta H$  is the film inhomogeneity line broadening, and  $\alpha$  is the damping parameter of the film. The damping  $\alpha$  of  $2.9 \times 10^{-3}$  and  $\mu_0 \Delta H$  of 8.2 mT are given by the linear fitting of the  $\delta f$  as a function of  $f$  (see Appendix B), which is comparable to the results of previous works [53]. The existence of the IrMn layer with large spin Hall angle will enhance the measured damping

$$f_{n=0} = \frac{|\gamma| \mu_0}{2\pi} \left[ \left( H_{\text{ext}} + H_{\text{ani}} \sin^2 \phi + \frac{2A}{\mu_0 M_s} k_{\parallel}^2 \right) \times \left( H_{\text{ext}} + H_{\text{ani}} \sin^2 \phi + \frac{2A}{\mu_0 M_s} k_{\parallel}^2 + F M_s \right) \right]^{\frac{1}{2}}, \quad (2)$$

$$F = 1 - \left( 1 - \frac{1 - e^{-k_{\parallel} t}}{k_{\parallel} t} \right) \cos^2 \theta + \left( \frac{M_s}{H_{\text{ext}} + H_{\text{ani}} \sin^2 \phi + \frac{2A}{\mu_0 M_s} k_{\parallel}^2} \right) \left( \frac{1 - e^{-2k_{\parallel} t}}{4} \right) \sin^2 \theta, \quad (3)$$

and for first-order mode it is given by [47,55,56]

$$f_{n=1} = \frac{|\gamma| \mu_0}{2\pi} \left( \left\{ H_{\text{ext}} + H_{\text{ani}} \sin^2 \phi + \frac{2A}{\mu_0 M_s} \left[ k_{\parallel}^2 + \left( \frac{n\pi}{t} \right)^2 \right] \right\} \times \left\{ H_{\text{ext}} + H_{\text{ani}} \sin^2 \phi + \frac{2A}{\mu_0 M_s} \left[ k_{\parallel}^2 + \left( \frac{n\pi}{t} \right)^2 \right] + M_s \right\} \right)^{\frac{1}{2}}, \quad (4)$$

where  $t = 80$  nm is the thickness of the CoFeB layer,  $n$  is the ordinal indices,  $\theta$  is the angle between the external magnetic field and wave vector direction, and  $\phi$  is the angle between field and easy axis, which is perpendicular to the wave vector  $k_{\parallel}$  directions in the experiments (in this case,  $\theta = \phi$ ). Equations (2) and (4) can nicely reproduce the field and angle dependent of the FMR spectra with fixing wave vector value  $k_{\parallel}$  as 0 rad/ $\mu\text{m}$  and  $n$  as 1 (see Appendix B). Through our analysis of the experimental results, we obtain that the saturation magnetization of 80-nm-thick CoFeB  $\mu_0 M_s$  is 2.14 T, the  $\mu_0 H_{\text{ani}}$  is 4 mT, and the exchange stiffness constant  $A$  is  $28 \times 10^{-12}$  J/m. It is worth noting that  $k_{\parallel}$  in Eqs. (2) and (4) denotes the in-plane wave vector and the uniaxial anisotropy is parallel to the exchange bias direction, which is induced by the applied bias field during sample growth process and perpendicular to the wave vector direction (see Appendixes A and B).

With the uniform excitation of the whole chip, the observed FMR and PSSW are separated well from each other (about 3 GHz). However, when we switch to using the NSL antenna, the narrow width of the NSL implies a broadband wave vector distribution, corresponding to a broad frequency range both in reflection and transmission spectra. The broader frequency range reaches its maximum at DE configuration and its minimum at the backwards volume (BV) configuration. If the NSL antenna provides broad enough wave vector distribution for the quasiuniform mode, it reaches the first-order mode at a certain angle  $\theta$  range between the DE and BV configuration. In addition, this antenna feature will also influence the PSSW mode, while the dispersion of this mode is relatively flat compared to the quasiuniform mode when the wave vector value is within the dipolar regime due to the absence of the dipolar term in Eq. (4). In previous works, it was shown that the first-order mode can also propagate along the in-plane direction without losing its fixed out-of-plane  $k_{\perp}$  (coherent

because it is also a path for energy dissipation via the spin pumping effect [54].

In order to extract the magnetic information of the sample from the field- and angle-dependent FMR spectra, we use the dispersion equation of dipole-exchange spin waves derived by Kalinikos and Slavin to fit these modes and extract helpful magnetic parameters [55–60]. In addition, the resonance frequencies of these two modes both present a sinusoidal dependence on the angle  $\theta$ , where the maximum frequencies appear at  $\pm 90^\circ$  (easy axis). Therefore, a uniaxial magnetic anisotropy field is also considered. The dispersion for the quasiuniform mode is given by

heterosymmetric spin waves) [46–49]. This has been experimentally imaged by time-resolved x-ray microscopy [47].

Inspired by these, we perform the angle-resolved propagating spin-wave spectroscopy (AR-PSWS) measurement, fixing the external magnetic field at 100 mT. Figures 1(c) and 1(d) show the angle-dependent spin-wave reflection and transmission spectra of the NSL antenna device, in which the white dashed curves are the fittings based on Eq. (2) with  $k_{\parallel}$  values of 0 and 2.5 rad/ $\mu\text{m}$ , and the red dashed curve is the fitting of the first-order mode by using Eq. (4). The transmission spectra  $S_{12}$  ( $S_{21}$ ) mean that spin waves are excited by NSL antenna 2 (1) and detected by NSL antenna 1 (2), respectively. As shown in Fig. 1(c), when the first-order and quasiuniform modes are crossing with each other, there is an obvious frequency range with almost zero intensity around the first-order mode. In the other way, for the transmission spectra [Fig. 1(d)], the first-order mode cuts across the transmission signal of the quasiuniform mode and the quasiuniform mode with  $k_{\parallel}$  of 2.5 rad/ $\mu\text{m}$  coherently couples with the first-order mode and generated two salient anticrossing gaps pointed at by the white arrows. To have a better presentation of the anticrossing gap, zoom-in spectra are shown in Fig. 1(f), where the quasiuniform mode (blue dashed line) becomes titled when crossing with the invisible first-order mode. Two curves sketched with blue-to-red transition color indicate the upper and bottom branches of the hybridized propagating modes formed by magnon-magnon coupling between the first-order and quasiuniform modes. To further understand the coupling between these two modes, we calculated and plotted their dispersions at different angles  $\theta$  as shown in Fig. 1(e) based on Eqs. (2) and (4). If one looks at the angular dependence, a clear anticrossing gap between quasiuniform mode with  $k_{\parallel}$  of 2.5 rad/ $\mu\text{m}$  and first-order mode is observed at  $36^\circ$  [Fig. 1(d)]. The dispersions at fixed angle  $\theta$  provide another perspective to understand this feature in wave vector space.

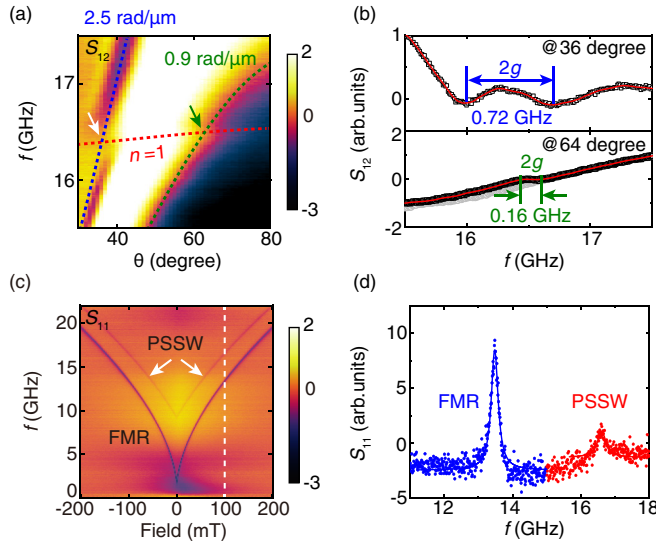


FIG. 2. (a) Zoom-in angle-dependent transmission spectra, where the red, blue, and green dashed lines are the theoretical fittings of the first-order and quasiuniform modes with wave vector values of 2.5 and 0.9 rad/ $\mu\text{m}$  by Eqs. (2) and (4), respectively. The white and green arrows point to the observed anticrossing gaps at 36° and 64°, respectively. (b) The extracted line plots at 36° and 64° with anticrossing gaps  $2g$  of 0.72 and 0.16 GHz, respectively, where the gray points are the moved experimental results if there is no coupling for better understanding. (c) The reflection spectra of the whole chip measured by flipchip technique with in-plane magnetic field. (d) The reflection spectrum line plot of FMR and PSSW extracted from (c) when the external magnetic field is 100 mT. The blue and red solid curve are the Lorentz fittings to extract the linewidths of these two modes.

For example, if the angle  $\theta$  is fixed at 36° [blue curve in Fig. 1(e)], the dispersions of these two modes cross at  $k_c = 2.5$  rad/ $\mu\text{m}$ , which is consistent with the angle-dependence data.

Besides the discussed anticrossing gap at 36°, a relative weak gap at 64° can also be found [Fig. 2(a)]. With the help of the two mode dispersions Eqs. (2) and (4), we find that the coupled quasiuniform mode wave vector value is 0.9 rad/ $\mu\text{m}$  at 64°, which is further reproduced and confirmed in Fig. 2(a) (green dashed curve). For further investigating the coupling mechanism between these two modes, we extract the transmission line plots at 36° and 64°, from which the anticrossing gaps of 0.76 and 0.16 GHz are observed for the coupling between the first-order and quasiuniform modes with different  $k_{\parallel}$  values of 2.5 and 0.9 rad/ $\mu\text{m}$ , respectively. If there were no coupling, the transmission would be continuous as shown by the light gray points in Fig. 2(b). The coupling strength  $g$  is defined as half of the peak-to-peak frequency difference in the anticrossing gap. In addition, we can also extract the dissipation rates for these two modes from the previous FMR measurements when the external magnetic field is 100 mT [Fig. 2(c)]. In addition, in Fig. 2(d), the solid curves are the Lorentz fittings of the FMR raw data at 100 mT. In terms of the extracted half widths at half maximum of the line broadenings, we obtained the  $\kappa_m^{\text{FMR}} = 0.26$  GHz and  $\kappa_m^{\text{PSSW}} = 0.31$  GHz, where the  $\kappa$  represents the dissipation rate. However, the obtained dissipation rate from the FMR mode ( $\kappa_m^{\text{FMR}}$ )

is not accurate because the coupled quasiuniform mode has the wave vector of 2.5 rad/ $\mu\text{m}$ , and the effective damping can be enhanced with the existence of nonzero wave vector  $k_{\parallel}$ . Therefore, based on the spin-wave phenomenological loss theory, an effective damping  $\alpha_{\text{eff}}$  is estimated, which is derived from the wave-vector-dependent relaxation time,

$$\begin{aligned} \tau(k_{\parallel}) &= \left( \alpha |\gamma| \mu_0 \left\{ H_{\text{ext}} + H_{\text{ani}} \sin^2 \phi + \frac{2A}{\mu_0 M_s} k_{\parallel}^2 \right. \right. \\ &\quad \left. \left. + \frac{M_s}{2} \left[ 1 - \left( 1 - \frac{1 - e^{-k_{\parallel} t}}{k_{\parallel} t} \right) \cos^2 \theta \right] \right\} \right)^{-1} \\ &= [2\pi \alpha_{\text{eff}} f_{n=0}(k_{\parallel})]^{-1}, \end{aligned} \quad (5)$$

where the  $\tau(k_{\parallel})$  is the spin-wave relaxation time at different wave vector values  $k_{\parallel}$ . After calculation based on Eq. (5), an effective damping  $\alpha_{\text{eff}}$  when the wave vector is 2.5 rad/ $\mu\text{m}$  is about  $5.5 \times 10^{-3}$ . Then, we can obtain the dissipation rate  $\kappa_m^{n=0} = 0.33$  GHz of the quasiuniform mode with considering the effective damping at 2.5 rad/ $\mu\text{m}$ . In this case, we achieve the strong coupling regime that  $g > \kappa_m^{n=0} > \kappa_m^{n=1}$ . The magnon-magnon cooperativity  $C$  is about 1.3 in our case based on the following equation [24]:

$$C = g^2 / \kappa_m^{n=1} \times \kappa_m^{n=0}. \quad (6)$$

The dispersions at different angles in Fig. 1(e) illustrate the crossing wave vector value  $k_c$  between the first-order and quasiuniform modes as a function of  $\theta$  (see Appendix C).  $k_c$  reaches its minimum value at DE configuration because the dipolar term in Eq. (2) enhances the group velocity of spin waves, causing the rapid increase of the quasiuniform mode frequency within the dipolar-dominant regime. With the transition from DE to BV mode (angle  $\theta$  goes away from 90°), the contribution of the dipolar term in Eq. (2) is suppressed. The crossing wave vector  $k_c$  is enhanced due to the smaller derivative of the dispersion. In addition, the maximum  $k_{\parallel}$  value observed in experiments is 3.0 rad/ $\mu\text{m}$  based on the theoretical calculation which reproduces the data in Fig. 1(d). In the other words, when  $\theta$  is smaller than 30° or larger than 150°, although these two modes can couple with each other, the required wave vector value  $k_{\parallel}$  cannot be achieved in the experiments due to the limited efficiency with which we can excite this  $k_{\parallel}$  value by using our NSL antenna. From the line plots presenting in Fig. 2(b), we can also find that the coupling strength is somewhat related to the value of  $k_c$  (see Appendix C).

Besides applying external fields with different angles, as discussed so far, we can also tune the value of the crossing wave vectors  $k_c$  by changing the external field strengths  $\mu_0 H_{\text{ext}}$ , owing to the interplay between the Zeeman energy and dipolar energy in Eq. (2) as shown in Fig. 3(a). Therefore, with the help of the field-dependent PSWS measurement, the relationship between the anticrossing gaps  $2g$  and  $k_c$  observed in the angle-dependent transmission spectra [Fig. 2(b)] can be further verified. For better observation, we start from the angle configuration with maximum strength of  $2g$  ( $\theta = 36^\circ$ ) and perform the field-dependent measurement by scanning the external magnetic field from 0 to 200 mT. In the field-dependent transmission spectra (see Appendix D), the anticrossing gap

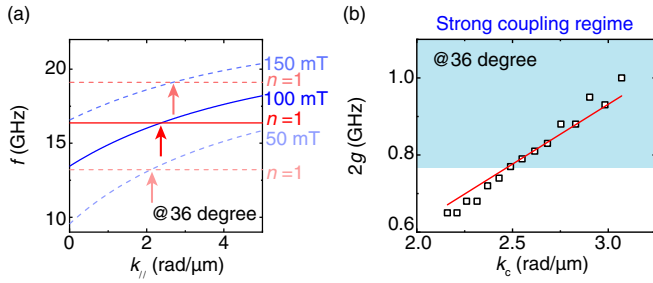


FIG. 3. (a) Theoretically calculated dispersions of first-order ( $n = 1$ ) and quasiuniform modes with different external magnetic field values but fixing the angle  $\theta$  of  $36^\circ$ , where the red arrows point to the crossing points. (b) The anticrossing gap as a function of the crossing wave vector values, where the blue shadow is the strong coupling regime and the red solid line is a linear fitting.

can be clearly observed as a cutoff around the frequency of the first-order mode. With increase of the external field strength, the Zeeman energy suppresses the influence of the dipolar term on the dispersion and makes it flatter within the dipolar-dominated regime and the crossing wave vector  $k_c$  is correspondingly enhanced as presented in Fig. 3(a). If the previous assumption is true that the coupling strength  $g$  is associate with the value of  $k_c$ , the maximum  $g$  can be obtained at 200 mT, the maximum field in our setup, and would be even larger at greater field values. We extract the anticrossing gap at each external field and plot them as the black open points as a function of  $k_c$  in Fig. 3(b), where a linear relationship is observed (red line is the linear fitting). This feature indicates again that, if the crossing wave vector value  $k_c$  between these two modes is larger, the coupling between them is stronger. In addition, one might be interested to know at which field value the coupling strength is in the strong coupling regime. Based on the field-dependent FMR spectra, we extract the dissipation rates of the first-order mode and calculate the dissipation rates of the quasiuniform mode with the help of Eqs. (1) and (5) (see Appendix D). When the field strength is above 100 mT, the coupling between first-order and quasiuniform modes is within the strong coupling regime. The largest cooperativity we can achieve is about 2.0 at 200 mT. It would be larger if stronger magnetic fields could be applied. If the field is smaller than 100 mT, the coupling is within weak coupling or magnetically induced transparency (MIT) regimes [24].

Now we discuss the key mechanism behind the observed linear relationship between the values of  $k_c$  and coupling strength. We show that it is the magnetic dipole-dipole interaction [42,55,56]. In these references, it was found that the hybridization between first-order and quasiuniform modes is induced by the off-diagonal contributions of dipolar origin (i.e., the dimensionless factors  $P_{nm}^{xy(yx)}$  for out-of-plane magnetized and  $Q_{nm'}^{xy(yx)}$  for in-plane magnetized with  $n = n'$ , where  $n = 0$  or 1 correspond to the quasiuniform and first-order modes; these parameters are defined in Ref. [56] and shown below). With following the theoretical formulation in Ref. [56], we recalculate the coupling between  $n = 0$  (quasiuniform) and  $n = 1$  (first-order) modes. If we assume the wave function of the  $n$ th mode of spin waves as  $m_n = (m_x^{(n)}, m_y^{(n)})^T$ ,

the system dynamic equations can be written as

$$\hat{D}_{nn} \cdot m_n + \sum_{n' \neq n} \hat{R}_{nn'} \cdot m_{n'} = 0. \quad (7)$$

In this case, the operators  $\hat{D}_{nn}$  and  $\hat{R}_{nn}$  are matrices, which can be written as

$$\hat{D}_{nn} = \begin{pmatrix} N_n + \sin^2 \beta + AP_{nn}, & -i(\frac{\omega}{\omega_M} - CQ_{nn}) \\ i(\frac{\omega}{\omega_M} + CQ_{nn}), & N_n + DP_{nn} \end{pmatrix}, \quad (8)$$

$$\hat{R}_{nn'} = \begin{pmatrix} AP_{nn'} + iBQ_{nn'}, & iCQ_{nn'}^{xy} \\ iCQ_{nn'}^{yx}, & DP_{nn'} \end{pmatrix}, \quad (9)$$

where  $\omega_M = |\gamma| \mu_0 M_s$ ,  $N_n$  is defined as follows,

$$N_n = \frac{H_{\text{ext}}}{M_s} + \frac{2A}{\mu_0 M_s^2} \left[ k_{\parallel}^2 + \left( \frac{n\pi}{t} \right)^2 \right], \quad (10)$$

and the geometrical factors of the system are defined as follows:

$$\begin{cases} A = \cos^2 \theta - \sin^2 \beta (1 + \cos^2 \theta), \\ B = -2 \cos \theta \sin 2\beta, \\ C = -2 \sin \beta \sin \theta, \\ D = \sin^2 \theta, \end{cases} \quad (11)$$

where the angle  $\beta$  represents the angle between the external magnetic field direction and film out-of-plane direction; therefore,  $\beta = 0$  represents the field applied along the out-of-plane direction and  $\beta = \pi/2$  represents in-plane direction, which fits our experiment configuration. Therefore, considering our measurement configuration, the parameters can be written as  $A = -1$ ,  $B = 0$ ,  $C = -2 \sin \theta$ , and  $D = \sin^2 \theta$ .

For diagonal factors, it could be easily calculated that  $Q_{nn} \equiv 0$ , and

$$P_{nn} = \begin{cases} \frac{k_{\parallel} t}{2}, & n = 0, \\ \left( \frac{k_{\parallel} t}{n\pi} \right)^2, & n \neq 0. \end{cases} \quad (12)$$

Now, we consider the off-diagonal factors,  $Q_{nn'}$  and  $P_{nn'}$ , of our system. We could calculate the exact quantity of these factors using the same definition within Ref. [56], then utilize the long-wave approximation ( $k_{\parallel} t \ll 1$ ) to simplify. We have already identified that the first-order mode is represented as the  $n = 1$  mode and the quasiuniform is represented as the  $n = 0$  mode. At this stage, we could focus specifically on those modes' off-diagonal factors according to Eqs. (A12) and (A13) in Ref. [56],

$$P_{01} = P_{10} = 0. \quad (13)$$

For the off-diagonal part  $Q_{01}$ , we claim that  $Q_{01}^{xy} = Q_{10}^{yx} = 0$ , whose calculation is displayed in Appendix E:

$$\begin{aligned} Q_{10}^{xy} &= -Q_{01}^{yx} = \frac{k_{\parallel}^2}{\sqrt{2} \left[ k_{\parallel}^2 + \left( \frac{\pi}{t} \right)^2 \right]^2} \cdot \left[ \frac{2}{k_{\parallel} t} - \frac{1}{2} \cdot \frac{2}{k_{\parallel} t} (1 - e^{-k_{\parallel} t}) \right] \\ &\cong \frac{\sqrt{2}}{\pi^2} \cdot k_{\parallel} t. \end{aligned} \quad (14)$$

It is worth noting that  $P_{00} = \frac{k_{\parallel} t}{2}$ , while for all other conditions under long-wave limit we have  $P_{nn} \sim O(k_{\parallel}^2) \rightarrow 0$ . At

this stage, we rewrite the dynamic equation operators,  $\hat{D}_{nm}$  and  $\hat{R}_{nm}$ , as

$$\hat{D}_{00} = \begin{pmatrix} N_0 + 1 - P_{00}, & -i \frac{\omega}{\omega_M} \\ i \frac{\omega}{\omega_M}, & N_0 + \sin^2 \theta \cdot P_{00} \end{pmatrix}, \quad (15)$$

$$\hat{D}_{11} = \begin{pmatrix} N_1 + 1, & -i \frac{\omega}{\omega_M} \\ i \frac{\omega}{\omega_M}, & N_1 \end{pmatrix}, \quad (16)$$

$$\hat{R}_{01} = \hat{R}_{10}^\dagger = \begin{pmatrix} 0, & -i \cdot 2 \sin \theta \cdot Q_{01}^{yx} \\ 0, & 0 \end{pmatrix}. \quad (17)$$

Then we can utilize the perturbation theory to approximately derive the dispersion formula near the anticrossing point within a small range. First, without hybridization effects (assuming that  $\hat{R}_{01} = 0$ ), we could calculate the basic state of our system according to Eqs. (44) and (52) in Ref. [56],

$$\left( \frac{\omega_0^{(0)}}{\omega_M} \right)^2 = (N_0 + 1 - P_{00}) \cdot (N_0 + \sin^2 \theta \cdot P_{00}), \quad (18)$$

$$\left( \frac{\omega_1^{(0)}}{\omega_M} \right)^2 = (N_1 + 1) \cdot N_1. \quad (19)$$

Here we write the  $n$ th-state perturbation-approximation frequency as  $\omega_{0(n)}^{(0)}$ . At the crossing point, we have  $\omega_0^{(0)} = \omega_1^{(0)}$ . Then, considering the first-state perturbation approximation, we have the secular equation according to Eq. (48) in Ref. [56],

$$\det \begin{pmatrix} \hat{D}_{00} & \hat{R}_{01} \\ \hat{R}_{10} & \hat{D}_{11} \end{pmatrix} = 0, \quad (20)$$

which could derive the approximate dispersion of the dipolar-dominant hybridization mode. Solving that equation, we derive that

$$\begin{aligned} (\omega_{\pm}^2 - \omega_0^{(0)2}) \cdot (\omega_{\pm}^2 - \omega_1^{(0)2}) &= 4\omega_M^4 \sin^2 \theta \cdot (Q_{01}^{yx})^2. \\ (N_0 + 1 - P_{00}) \cdot N_1 &= [\Delta(\omega_{\pm}^2)/2]^2. \end{aligned} \quad (21)$$

Due to the Taylor expansion of the frequency,

$$\Delta\omega_{\pm} = \frac{1}{2\omega_0^{(0)}} \Delta(\omega_{\pm}^2). \quad (22)$$

Under the long-wave limit, based on Eqs. (18) and (19), one can find that  $N_0$  is approximately equal to  $N_1$  (see Appendix E). Therefore, Eq. (22) can be approximately simplified as

$$\Delta\omega_{\pm} = 2\omega_M \cdot \sin \theta \cdot Q_{01}^{yx} = \frac{2\sqrt{2}}{\pi^2} \omega_M \cdot \sin \theta \cdot k_{\parallel} t. \quad (23)$$

Based on these calculations, the hybridization gap is found to be proportional to  $Q_{01} \propto k_c$  under long-wave approximation, which is consistent with our observation as shown in Fig. 3(b). The red solid line is the linear fitting of the experimental data extracted from field-dependent transmission spectra. The observed difference between the experimental results and the linear fitting in Fig. 3(b) might be due to the fact that the spin waves in our system are deviating slightly from the deep long-wave limit regime ( $k_{\parallel} t \approx 0.2$ ). Therefore, the higher-order terms and the direct effect of dipolar

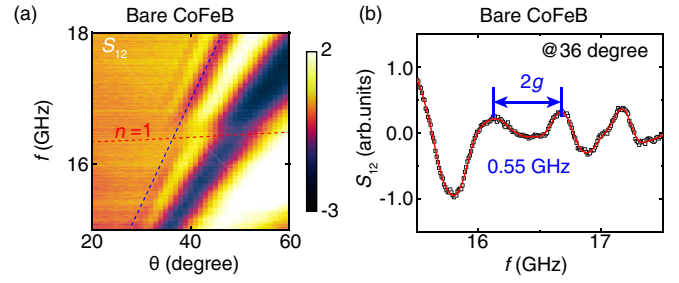


FIG. 4. (a) Zoom-in angle-dependent transmission spectra at 100 mT on a pure CoFeB film 80 nm thick. (b) Line plot extracted from Fig. 4(a) (imaginary part of  $S_{12}$ ) at  $\theta$  of  $36^\circ$  to figure out the contribution of IrMn layer.

coupling begin to contribute into the relationship between  $2g$  and  $k_c$ , where another term proportional to  $(k_c t)^2$  comes up. Therefore, based on these, the theoretical analysis nicely accounts for the observed features in our experiments, whose key mechanism is dipole-dipole interaction.

At last, a reference sample (pure CoFeB with the same thickness but without IrMn layer) is grown by using the same growth condition to qualitatively illustrate the contribution from the IrMn layer in the observed hybridized propagating spin waves. Figure 4(a) shows the zoom-in anticrossing gap spectra under the same configuration of Fig. 1(f), where the two modes still couple and generate an anticrossing gap at  $36^\circ$ . The line plot at  $36^\circ$  is extracted and shown in Fig. 4(b). Compared to Fig. 2(b), the extracted anticrossing gap  $2g$  without 10-nm-thick IrMn is about three-quarters of the one with IrMn. Therefore, we suppose that the CoFeB/IrMn interface helps the formation of the first-order (PSSW) mode, which needs strong pinning at the surface, and therefore enhances the coupling strength via interfacial exchange-bias effect [48, 50–52]. Further detailed IrMn thickness dependence experiments would be interesting but beyond the scope of this study.

#### IV. CONCLUSION

In conclusion, we excited and detected hybridized propagating spin waves in an 80-nm-thick CoFeB layer capped by 10-nm-thick IrMn at room temperature. By utilizing the AR-PSWS and NSL antennas with a broadband distribution of  $k_{\parallel}$  values, angle-dependent spin-wave transmission and reflection spectra are measured, from which we are able to clearly observe the anticrossing gaps between the quasi-uniform and first-order spin-wave modes. Calculations based on the dipole-exchange spin-wave dispersions by using the magnetic parameters extracted from FMR measurements are provided to figure out the coupling wave vector values. Interestingly, the anticrossing gaps present different values when changing the angles  $\theta$  between the applied magnetic field and the  $k_{\parallel}$  vector of the microwave as the wave vector at the crossing of the dispersion curves for both modes is also changing. In addition to varying magnetic field orientation, we find a systematic way to change the crossing wave vector values by applying different field strengths at a fixed angle (the stronger the field, the larger the crossing wave vector values). After extracting anticrossing gaps with respect to crossing wave vector values, a linear relationship between gap and  $k_{\parallel}$  values is

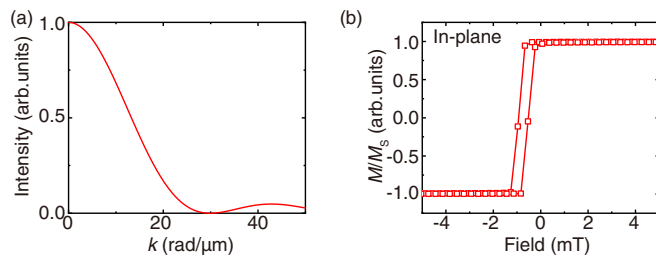


FIG. 5. (a) Wave vector distribution of the NSL antenna shown in Fig. 1(b) in the main text calculated by FFT from spatial space. (b) The magnetic hysteresis loop measured by VSM with applying an in-plane magnetic field along the exchange-bias (pinning) direction.

experimentally observed and explained by using the theoretical method of Ref. [56], where the key mechanism of the coupling between these two modes is an off-diagonal contribution of the dipolar origin. Finally, when the same measurements are conducted using a CoFeB layer without IrMn capping, the coupling strength is weaker compared to the sample capped by IrMn. Our results provide experimental insight for hybridized magnonics on a magnetic system widely used in spintronics.

#### ACKNOWLEDGMENTS

The authors acknowledge support from the National Key Research and Development Program of China, Grants No. 2017YFA0206200 and No. 2016YFA0300802, the NSF China under Grants No. 12074026, No. 12104208, and No. U1801661, and the 111 Talent Program B16001.

#### APPENDIX A: IN-PLANE MAGNETIC HYSTERESIS LOOP AND WAVE VECTOR DISTRIBUTION OF THE NSL ANTENNA

The wave vector distribution of the 200-nm-wide NSL antenna is calculated by the fast Fourier transformation (FFT), which shows a broadband distribution starting from uniform precession [Fig. 5(a)]. The broadband wave vector can easily cover the observed crossing wave vector values between first-order and quasiuniform modes at different angles  $\theta$  and field strengths. We use the vibrating sample magnetometer (VSM) measurement to characterize the magnetic hysteresis loop along its pinning direction (easy axis) with in-plane magnetic fields. From Fig. 5(b), we can observe a clear squared hysteresis loop with about 1 mT exchange bias induced by the IrMn layer.

#### APPENDIX B: FIELD- AND ANGLE-DEPENDENT FMR SPIN-WAVE SPECTRA AND DAMPING ESTIMATION

Before performing the propagating spin-wave measurements, we first use the flipchip measurement, where the submillimeter size coplanar waveguide (CPW) antenna is used to excite and detect the resonance of the whole chip, to characterize the FMR feature of the sample. With applying an in-plane external magnetic field along the antenna strips

direction, which is parallel to the pinning direction (easy axis) of the CoFeB/IrMn but perpendicular to the wave vector direction of the large CPW [Damon-Eshbach (DE) configuration], a field-dependent spectra is obtained by scanning the field value from  $-200$  to  $200$  mT with a step of 2 mT as presented in Fig. 6(a). There are two salient modes existing in Fig. 6(a). One is the FMR of CoFeB with stronger intensity but lower frequency and the other one is the PSSW mode with lower intensity but higher frequency. As shown in Fig. 6(c), we zoom in Fig. 6(a) around 0 mT, where an asymmetry frequency dependent with respect to the field around 0 field is observed (white arrows). In addition, when the field is 0 mT, the FMR and PSSW modes can still be observed in the spectra, indicating that the IrMn layer can bias the CoFeB layer and influence the symmetry of the signal when the external magnetic field strength is relatively small, because the exchange bias field is only about 1 mT. Based on the FMR spectra of CoFeB, the linewidths  $\delta f$  at different excitation frequencies are extracted by fitting with a Lorentz function [Fig. 6(d)]. We estimate the damping parameter of the film by using the following Eq. (1) in the main text. The damping  $\alpha$  of  $2.94 \times 10^{-3}$  and  $\mu_0 \Delta H$  of 8.2 mT are given by the linear fitting in Fig. 6(d).

To obtain more information on this sample, we fix the external magnetic field at 100 mT and rotate the field direction with respect to the wave vector direction of the excitation antenna, where the angle between field and wave vector is defined as  $\theta$ . Two observed modes are reproduced in the angle-dependent FMR spectra as shown in Fig. 6(b). The resonance frequencies of these two modes both present a sinusoidal dependence on the angle  $\theta$ , where the maximum frequencies are appearing at  $\pm 90^\circ$ , which is along the easy axis of the CoFeB which is determined by the exchange biasing obtained during sample preparation. In order to extract the sample magnetic information from the field- and angle-dependent FMR spectra, we use the dispersion equation of dipole-exchange spin waves derived by Kalinikos and Slavin to fit and extract information helpful with considering a uniaxial magnetic anisotropy field [Eqs. (2)–(4) in the main text].

As presented in Figs. 6(e) and 6(f), Eqs. (2)–(4) in the main text can nicely reproduce the field and angle dependent of the first-order and quasiuniform mode with fixing wave vector value  $k$  as  $0 \text{ rad}/\mu\text{m}$  and  $n$  as 1. Through our analysis of the experimental results, we obtain that the saturation magnetization of 80-nm-thick CoFeB  $\mu_0 M_S$  is 2.14 T, the  $\mu_0 H_{\text{ani}}$  is 4 mT, and the exchange stiffness constant  $A$  is  $28 \times 10^{-12} \text{ J/m}$ .

#### APPENDIX C: CALCULATED ANGLE-DEPENDENT MODE FREQUENCIES AND CROSSING WAVE VECTOR VALUE $k_c$

It is worth noting that the first-order mode not only couples with the  $2.5 \text{ rad}/\mu\text{m}$  quasiuniform mode at  $36^\circ$  but also the other quasiuniform modes with different wave vector values within the broadband provided by the NSL. If we understand the modes' dispersion from the angular space viewpoint, the calculated frequencies of the quasiuniform modes with  $k$  equaling 0.5, 1.0, 2.0, and  $3.0 \text{ rad}/\mu\text{m}$  as a function of the

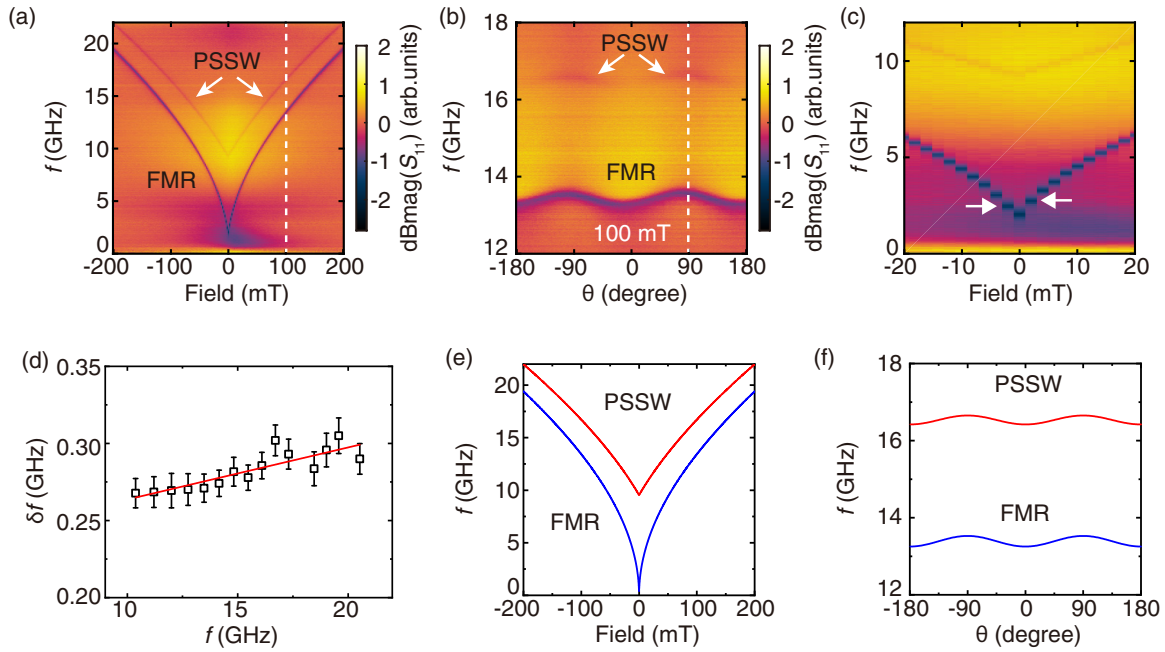


FIG. 6. (a) FMR reflection spectra measured by flipchip technique with in-plane magnetic field. (b) The angle-dependent FMR reflection spectra measured by flipchip with fixing the in-plane magnetic field at 100 mT. (c) The zoom-in spectra of (a) to present the influence of exchange bias on the CoFeB layer. (d) The extracted FMR linewidths  $\delta f$  as a function of the different excitation frequencies. The red solid line is the damping fitting based on Eq. (1) in the main text. (e),(f) Theoretically calculated field- and angle-dependent FMR and PSSW spectra based on Eqs. (2) and (4) in the main text.

angle  $\theta$  are plotted in Fig. 7(a), from which one can find that the curves with 1.0, 2.0, and 3.0  $\text{rad}/\mu\text{m}$  will also cross with the first-order mode, just with different crossing angles.

Besides the angular space viewpoint, the dispersions at fixed angle  $\theta$  provide another angle of view to understand this feature in wave vector space. For example, if the angle  $\theta$  is fixed at  $36^\circ$  [blue curve in Fig. 1(e) in the main text], the dispersion of these two modes cross at  $k_c = 2.5 \text{ rad}/\mu\text{m}$ , which is consistent with the angle-dependence data. Based on these, we extract the wave vector values of the quasiuniform mode coupled with the first-order mode at each angle  $\theta$ , from the  $k$  space, namely, the crossing wave vector  $k_c$  between two modes as a function of  $\theta$ . As shown by the

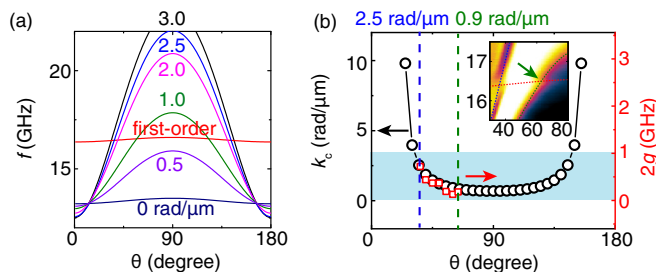


FIG. 7. (a) Theoretical fittings of angle-dependent first-order and quasiuniform modes with different wave vectors reproduce the observed spectra profile shown in Figs. 1(c) and 1(d) in the main text. (b) The crossing wave vector  $k_c$  as a function of the angle between field and wave vector  $\theta$ . The red points are the anticrossing gaps extracted from Fig. 1(d) at other angles. The inset shows the relative weak anticrossing gap at  $64^\circ$  corresponding to the quasiuniform with  $0.9 \text{ rad}/\mu\text{m}$ .

black points in Fig. 7(b),  $k_c$  is minimum at the DE mode configuration because the dipolar term in Eqs. (2) and (3) in the main text enhances the group velocity of spin waves, causing the rapid increase of the quasiuniform frequency within the dipolar-dominant regime. With the transition from DE to BV mode (angle  $\theta$  goes away from  $90^\circ$ ), the contribution of the dipolar term in Eqs. (2) and (3) in the main text is suppressed. The crossing wave vector  $k_c$  is enhanced due to the smaller derivative of the dispersion. In addition, the maximum  $k$  value observed in experiments is  $3.0 \text{ rad}/\mu\text{m}$  based on the theoretical predication reproducing the data of Fig. 7(a). In other words, when  $\theta$  is smaller than  $30^\circ$  or larger than  $150^\circ$ , although these two modes can couple with each other, the required wave vector value  $k$  cannot be achieved in the experiments due to the limited efficient excitation in the  $k$  broadband imposed by the NSL antenna. The shadow in Fig. 7(b) indicates the observed wave vector range in the experiment. If we look further into the transmission spectra, there is also a minianticrossing happening at  $64^\circ$  as the green arrow pointed in the inset of Fig. 7(b), where the green dashed curve is the angle-dependent quasiuniform mode with  $k$  of  $0.9 \text{ rad}/\mu\text{m}$  by the theoretical calculation. To extract the coupling strength at  $64^\circ$ , the transmission spectrum is plotted in Fig. 2(b) in the main text, where the anticrossing stops the signal to continue going up and generating a frequency range  $2g$  of about  $0.16 \text{ GHz}$ . By using the same data treatment method, we summarize the gap strengths (twice of the coupling strength  $g$ ) as the red points plotted together with  $k_c$  from  $36^\circ$  to  $64^\circ$  in Fig. 7(b). Interestingly, the trend between the coupling strength and angle  $\theta$  seems to be the same as that of the crossing wave vector  $k_c$ , namely, the coupling strength somehow is related to the value of  $k_c$ .

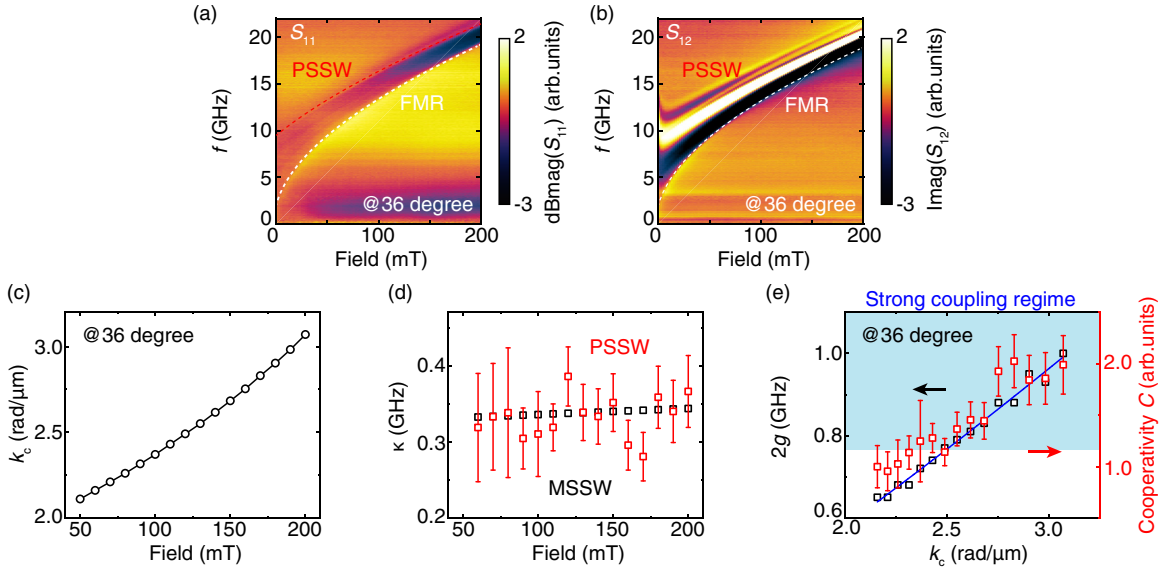


FIG. 8. (a),(b) Field-dependent reflection and transmission spectra measured at  $\theta$  of  $36^\circ$  configuration, where the white and red dashed lines are the theoretical calculation of the FMR and first-order modes, respectively. (c) The wave vector crossing points as a function of the external magnetic fields at  $36^\circ$ . (d) The extracted and calculated dissipation rates of first-order and quasiuniform modes at different external magnetic field. (e) The anticrossing gap and calculated cooperativity as a function of the crossing wave vector values, where the blue shadow is the guide of strong coupling regime for the eye and the blue solid line is the theoretical fitting.

#### APPENDIX D: FIELD-DEPENDENT REFLECTION AND TRANSMISSION SPIN-WAVE SPECTRA AT $36^\circ$

Besides the measurement configuration (the change of  $\theta$ ), the external field strength  $\mu_0 H_{\text{ext}}$  also influences the dispersion of the quasiuniform mode due to the interplay between the Zeeman energy and dipolar energy in Eqs. (2) and (3) in the main text. Therefore, with the help of the field-dependent PSWS measurement, the relationship between the coupling strength  $g$  and  $k_c$  observed in the angle-dependent transmission spectra [Fig. 7(b)] can be further verified. For better observation, we start from the angle configuration with maximum strength of  $g$  ( $\theta = 36^\circ$ ) and perform the field-dependent measurement by scanning the external magnetic field from 0 to 200 mT. Figures 8(a) and 8(b) are the reflection and transmission spectra measured by fixing the angle  $\theta$  at  $36^\circ$ , where the white dashed curves are the quasiuniform FMR fitting and the red dashed curve is the calculated field-dependent first-order mode. In these two spectra, the anticrossing gap can be obviously observed as a cut off around the frequency of first-order mode. From the wave vector  $k$  space, with the increase of the external field strength, the Zeeman energy suppresses the influence from the dipolar term on the dispersion and makes it flatter within the dipolar-dominated regime, and the crossing wave vector  $k_c$  is correspondingly enhanced as presented in Fig. 3(a) in the main text. The crossing point  $k_c$  as a function of field strength is extracted in Fig. 8(c), where the  $k_c$  increases with the larger field. If the previous assumption is true that the coupling strength  $g$  is associated with the value of  $k_c$ , the maximum  $g$  can be obtained at 200 mT, and even larger above 200 mT.

With this expectation, we extract the anticrossing gaps at each external field and plot them as the black open points as a function of  $k_c$  in Fig. 3(b), where a linear

relationship is observed (blue line is the linear fitting). This feature indicates again that, if the crossing wave vector value  $k_c$  between the dispersions of first-order and quasiuniform modes is larger, the coupling between them is stronger. In addition, one might be interested to know at which field value the coupling strength is in the strong coupling regime. Based on the field-dependent FMR spectra [Fig. 2(c) in the main text], we extract the dissipation rates of the first-order mode and calculate the dissipation rates of the quasiuniform mode with the help of Eqs. (1) and (5) in the main text at each magnetic field [Fig. 8(d)]. By using Eq. (6) in the main text, the cooperativity  $C$  with considering the error bars of the first-order mode  $\kappa_m^{n=1}$  is also estimated at different values of  $k_c$ , which presents the same trend ( $\propto k_c$ ). When the field strength is above 100 mT, the coupling between first-order and quasiuniform modes is within the strong coupling regime, of which the cooperativity will be further enhanced with larger magnetic field strength.

#### APPENDIX E: DERIVATION OF THEORETICAL PARAMETERS

Considering the boundary conditions, according to Eq. (12) in Ref. [56] (all the definitions below are the same as those in Ref. [56]), we could get the eigenvalues of the dynamic equations obey that

$$\begin{pmatrix} \frac{\partial}{\partial \xi} - (-1)^\alpha d_\alpha \cos 2\beta & 0 \\ 0 & \frac{\partial}{\partial \xi} - (-1)^\alpha d_\alpha \cos \beta^2 \end{pmatrix} \times \begin{pmatrix} \Phi_{x,n} \\ \Phi_{y,n} \end{pmatrix} = 0, \quad (\text{E1})$$

where  $\alpha = \{1, 2\}$  and  $n$  is in the range that  $n \neq 0$ , and  $d_\alpha$  are the pinning parameters on the upper and lower surfaces of the

film. With specifically our system's parameter,  $\beta = \pi/2$ , from this equation we could derive that

$$\frac{\partial}{\partial \xi} \Phi_{y,1} = 0. \quad (\text{E2})$$

In addition, when  $n \neq 0$ , there are only standing wave solutions to the dynamic equations, which implies that  $\Phi_y = 0$ . From Eq. (26) in Ref. [56], we could calculate the off-diagonal parameter as

$$Q_{01}^{xy} = -Q_{10}^{yx} = \int_{-\frac{l}{2}}^{\frac{l}{2}} \frac{1}{2t} \cdot G_Q \Phi_{x,0} \Phi_{y,1} d\mathbf{r} = 0 \quad (\text{E3})$$

and then we could write down the equations of perturbation as

$$\det \begin{pmatrix} \hat{D}_{00} & 0 & 0 \\ 0 & i \cdot 2 \sin \theta \cdot Q_{01}^{yx} & 0 \\ 0 & 0 & \hat{D}_{11} \end{pmatrix} = 0. \quad (\text{E4})$$

In addition, within our essay, we could have the relation between  $N_0$  and  $N_1$  as

$$\left( \frac{\omega_0^{(0)}}{\omega_M} \right)^2 = (N_0 + 1 - P_{00}) \cdot (N_0 + \sin^2 \theta \cdot P_{00}) \quad (\text{E5})$$

and

$$\left( \frac{\omega_1^{(0)}}{\omega_M} \right)^2 = (N_1 + 1) \cdot N_1. \quad (\text{E6})$$

Then, when  $\omega_0^{(0)} = \omega_1^{(0)}$ , the deviation between the upper two equations indicates that

$$(N_1 + 1) \cdot N_1 = (N_0 + 1 - P_{00}) \cdot (N_0 + \sin^2 \theta \cdot P_{00}), \quad (\text{E7})$$

then

$$(N_1 + 1) \cdot N_1 - (N_0 + 1) \cdot N_0 = P_{00} \cdot (N_0 + \sin^2 \theta \cdot P_{00}) - (N_0 + 1) \cdot \sin^2 \theta \cdot P_{00}, \quad (\text{E8})$$

which could be further simplified as

$$N_0 - N_1 = \frac{\sin^2 \theta - N_0 \cos^2 \theta}{N_0 + N_1 + 1} \cdot P_{00} \sim kt. \quad (\text{E9})$$

- 
- [1] A. Frisk Kockum, A. Miranowicz, S. De Liberato, S. Savasta, and F. Nori, Ultrastrong coupling between light and matter, *Nat. Rev. Phys.* **1**, 19 (2019).
- [2] A. Imamoglu, Cavity QED Based on Collective Magnetic Dipole Coupling: Spin Ensembles as Hybrid Two-Level Systems, *Phys. Rev. Lett.* **102**, 083602 (2009).
- [3] X. Zhu, S. Saito, A. Kemp, K. Kakuyanagi, S.-I. Karimoto, H. Nakano, W. J. Munro, Y. Tokura, M. S. Everitt, K. Nemoto, M. Kasu, N. Mizuochi, and K. Semba, Coherent coupling of a superconducting flux qubit to an electron spin ensemble in diamond, *Nature (London)* **478**, 221 (2011).
- [4] Y. Tabuchi, S. Ishino, A. Noguchi, T. Ishikawa, R. Yamazaki, K. Usami, and Y. Nakamura, Coherent coupling between a ferromagnetic magnon and a superconducting qubit, *Science* **349**, 405 (2015).
- [5] M. Aspelmeyer, T. J. Kippenberg, and F. Marquardt, Cavity optomechanics, *Rev. Mod. Phys.* **86**, 1391 (2014).
- [6] P. Pirro, V. I. Vasyuchka, A. A. Serga, and B. Hillebrands, Advances in coherent magnonics, *Nat. Rev. Mater.* **6**, 1114 (2021).
- [7] D. D. Stancil and A. Prabhakar, *Spin Waves: Theory and Applications* (Springer, New York, 2009), Appendix C.
- [8] A. V. Chumak, V. I. Vasyuchka, A. A. Serga, and B. Hillebrands, Magnon spintronics, *Nat. Phys.* **11**, 453 (2015).
- [9] V. Vlaminck and M. Bailleul, Current-induced spin-wave Doppler shift, *Science* **322**, 410 (2008).
- [10] H. Yu, J. Xiao, and H. Schultheiss, Magnetic texture based magnonics, *Phys. Rep.* **905**, 1 (2021).
- [11] L. Caretta, S.-H. Oh, T. Fakhru, D.-K. Lee, B. H. Lee, S. K. Kim, C. Ross, K.-J. Lee, and G. S. D. Beach, Relativistic kinematics of a magnetic soliton, *Science* **370**, 1438 (2021).
- [12] G. Csaba, A. Papp, and W. Porod, Perspectives of using spin waves for computing and signal processing, *Phys. Lett. A* **381**, 1471 (2017).
- [13] V. V. Kruglyak, S. O. Demokritov, and D. Grundler, Magnonics, *J. Phys. D* **43**, 264001 (2010).
- [14] K. Vogt, F. Y. Fradin, J. E. Pearson, T. Sebastian, S. D. Bader, B. Hillebrands, A. Hoffmann, and H. Schultheiss, Realization of a spin-wave multiplexer, *Nat. Commun.* **5**, 3727 (2014).
- [15] A. Barman, G. Gubbiotti, S. Ladak *et al.*, The 2021 magnonics roadmap, *J. Phys.: Condens. Matter* **33**, 413001 (2021).
- [16] B. Z. Rameshti, S. V. Kusminskiy, J. A. Haigh, K. Usami, D. Lachance-Quirion, Y. Nakamura, C.-M. Hu, H. X. Tang, G. E. W. Bauer, and Y. M. Blanter, Cavity magnonics, *Phys. Rep.* **979**, 1 (2022).
- [17] Y. Li, W. Zhang, V. Tyberkevych, W.-K. Kwok, A. Hoffmann, and V. Novosad, Hybrid magnonics: Physics, circuits, and applications for coherent information processing, *J. Appl. Phys.* **128**, 130902 (2020).
- [18] M. Elyasi, Y. M. Blanter, and G. E. W. Bauer, Resources of nonlinear cavity magnonics for quantum information, *Phys. Rev. B* **101**, 054402 (2020).
- [19] L. Bai, M. Harder, P. Hyde, Z. Zhang, C.-M. Hu, Y. P. Chen, and J. Q. Xiao, Cavity Mediated Manipulation of Distant Spin Currents using a Cavity-Magnon-Polariton, *Phys. Rev. Lett.* **118**, 217201 (2017).
- [20] L. H. Bai, M. Harder, Y. P. Chen, X. Fan, J. Q. Xiao, and C. M. Hu, Spin Pumping in Electrodynamically Coupled Magnon-Photon Systems, *Phys. Rev. Lett.* **114**, 227201 (2015).
- [21] M. Mergenthaler, J. Liu, J. J. Le Roy, N. Ares, A. L. Thompson, L. Bogani, F. Luis, S. J. Blundell, T. Lancaster, A. Ardavan, G. A. D. Briggs, P. J. Leek, and E. A. Laird, Strong Coupling

- of Microwave Photons to Antiferromagnetic Fluctuations in an Organic Magnet, *Phys. Rev. Lett.* **119**, 147701 (2017).
- [22] Y. Li, T. Polakovic, Y. L. Wang, J. Xu, S. Lendinez, Z. Zhang, J. Ding, T. Khaire, H. Saglam, R. Divan, J. Pearson, W. K. Kwok, Z. L. Xiao, V. Novosad, A. Hoffmann, and W. Zhang, Strong Coupling between Magnons and Microwave Photons in On-Chip Ferromagnet-Superconductor Thin-Film Devices, *Phys. Rev. Lett.* **123**, 107701 (2019).
- [23] J. T. Hou and L. Q. Liu, Strong Coupling between Microwave Photons and Nanomagnet Magnons, *Phys. Rev. Lett.* **123**, 107702 (2019).
- [24] X. Zhang, C.-L. Zou, L. Jiang, and H. X. Tang, Strongly Coupled Magnons and Cavity Microwave Photons, *Phys. Rev. Lett.* **113**, 156401 (2014).
- [25] X. Zhang, C.-L. Zou, N. Zhu, F. Marquardt, L. Jiang, and H. X. Tang, Magnon dark modes and gradient memory, *Nat. Commun.* **6**, 8914 (2015).
- [26] H. Huebl, C. W. Zollitsch, J. Lotze, F. Hocke, M. Greifenstein, A. Marx, R. Gross, and S. T. B. Goennenwein, High Cooperativity in Coupled Microwave Resonator Ferrimagnetic Insulator Hybrids, *Phys. Rev. Lett.* **111**, 127003 (2013).
- [27] Y. Tabuchi, S. Ishino, T. Ishikawa, R. Yamazaki, K. Usami, and Y. Nakamura, Hybridizing Ferromagnetic Magnons and Microwave Photons in the Quantum Limit, *Phys. Rev. Lett.* **113**, 083603 (2014).
- [28] M. Bialek, J. Zhang, H. Yu, and J.-P. Ansermet, Strong Coupling of Antiferromagnetic Resonance with Subterahertz Cavity Fields, *Phys. Rev. Applied* **15**, 044018 (2021).
- [29] H. Man, Z. Shi, G. Xu, Y. Xu, X. Chen, S. Sullivan, J. Zhou, K. Xia, J. Shi, and P. Dai, Direct observation of magnon-phonon coupling in yttrium iron garnet, *Phys. Rev. B* **96**, 100406(R) (2017).
- [30] B. Casals, N. Statuto, M. Foerster, A. Hernández-Mínguez, R. Cicheler, P. Manshausen, A. Mandziak, L. Aballe, J. M. Hernández, and F. Macià, Generation and Imaging of Magnetoacoustic Waves over Millimeter Distances, *Phys. Rev. Lett.* **124**, 137202 (2020).
- [31] S. Liu, A. Granados del Aguila, D. Bhowmick, C. K. Gan, T. Thu Ha Do, M. A. Prosnikov, D. Sedmidubsky, Z. Sofer, P. C. M. Christianen, P. Sengupta, and Q. Xiong, Direct Observation of Magnon-Phonon Strong Coupling in Two-Dimensional Antiferromagnet at High Magnetic Fields, *Phys. Rev. Lett.* **127**, 097401 (2021).
- [32] C. Berk, M. Jaris, W. Yang, S. Dhuey, S. Cabrini, and H. Schmidt, Strongly coupled magnonphonon dynamics in a single nanomagnet, *Nat. Commun.* **10**, 2652 (2019).
- [33] M. Kuss, M. Heigl, L. Flacke, A. Horner, M. Weiler, M. Albrecht, and A. Wixforth, Nonreciprocal Dzyaloshinskii-Moriya Magnetoacoustic Waves, *Phys. Rev. Lett.* **125**, 217203 (2020).
- [34] J. Y. Zhang, M. F. Chen, J. L. Chen, K. Yamamoto, H. C. Wang, M. Hamdi, Y. W. Sun, K. Wagner, W. Q. He, Y. Zhang, J. Ma, P. Gao, X. F. Han, D. P. Yu, P. Maletinsky, J. P. Ansermet, S. Maekawa, D. Grundler, C. W. Nan, and H. M. Yu, Long decay length of magnon-polarons in  $\text{BiFeO}_3 \text{La}_{0.67} \text{Sr}_{0.33} \text{MnO}_3$  heterostructures, *Nat. Commun.* **12**, 7258 (2021).
- [35] D. Lachance-Quirion, S. P. Wolski, Y. Tabuchi, S. Kono, K. Usami, and Y. Nakamura, Entanglement-based single-shot detection of a single magnon with a superconducting qubit, *Science* **367**, 425 (2020).
- [36] S. P. Wolski, D. Lachance-Quirion, Y. Tabuchi, S. Kono, A. Noguchi, K. Usami, and Y. Nakamura, Dissipation-Based Quantum Sensing of Magnons with a Superconducting Qubit, *Phys. Rev. Lett.* **125**, 117701 (2020).
- [37] A. Gloppe, M. Onga, R. Hisatomi, A. Imamoglu, Y. Nakamura, Y. Iwasa, and K. Usami, Magnon-exciton proximity coupling at a van der Waals heterointerface, *Phys. Rev. B* **105**, L121403 (2022).
- [38] L. Liensberger, A. Kamra, H. Maier-Flaig, S. Geprags, A. Erb, S. T. B. Goennenwein, R. Gross, W. Belzig, H. Huebl, and M. Weiler, Exchange-Enhanced Ultrastrong Magnon-Magnon Coupling in a Compensated Ferrimagnet, *Phys. Rev. Lett.* **123**, 117204 (2019).
- [39] Y. Shiota, T. Taniguchi, M. Ishibashi, T. Moriyama, and T. Ono, Tunable Magnon-Magnon Coupling Mediated by Dynamic Dipolar Interaction in Synthetic Antiferromagnets, *Phys. Rev. Lett.* **125**, 017203 (2020).
- [40] J. L. Chen, C. P. Liu, T. Liu, Y. Xiao, K. Xia, G. E. W. Bauer, M. Z. Wu, and H. M. Yu, Strong Interlayer Magnon-Magnon Coupling in Magnetic Metal-Insulator Hybrid Nanostructures, *Phys. Rev. Lett.* **120**, 217202 (2018).
- [41] H. J. Qin, S. J. Hämäläinen, and S. V. Dijken, Exchange-torque-induced excitation of perpendicular standing spin waves in nanometer-thick YIG films, *Sci. Rep.* **8**, 5755 (2018).
- [42] S. Tacchi, R. Silvani, G. Carlotti, M. Marangolo, M. Eddrief, A. Rettori, and M. G. Pini, Strongly hybridized dipole-exchange spin waves in thin Fe-N ferromagnetic films, *Phys. Rev. B* **100**, 104406 (2019).
- [43] A. Sud, C. W. Zollitsch, A. Kamimaki, T. Dion, S. Khan, S. Iihama, S. Mizukami, and H. Kurebayashi, Tunable magnon-magnon coupling in synthetic antiferromagnets, *Phys. Rev. B* **102**, 100403(R) (2020).
- [44] W. Song, X. Wang, C. Jia, X. Wang, C. Jiang, D. Xue, and G. Chai, Nonreciprocal emergence of hybridized magnons in magnetic thin films, *Phys. Rev. B* **104**, 014402 (2021).
- [45] S. Klingler, V. Amin, S. Geprags, K. Ganzhorn, H. Maier-Flaig, M. Althammer, H. Huebl, R. Gross, R. D. McMichael, M. D. Stiles, S. T. B. Goennenwein, and M. Weiler, Spin-Torque Excitation of Perpendicular Standing Spin Waves in Coupled YIG/Co Heterostructures, *Phys. Rev. Lett.* **120**, 127201 (2018).
- [46] A. Navabi, C. Chen, A. Barra, M. Yazdani, G. Yu, M. Montazeri, M. Aldosary, J. Li, K. Wong, Q. Hu, J. Shi, G. P. Carman, A. E. Sepulveda, P. Khalili Amiri, and K. L. Wang, Efficient Excitation of High-Frequency Exchange-Dominated Spin Waves in Periodic Ferromagnetic Structures, *Phys. Rev. Applied* **7**, 034027 (2017).
- [47] G. Dieterle, J. Forster, H. Stoll, A. S. Semisalova, S. Finizio, A. Gangwar, M. Weigand, M. Noske, M. Fahnle, I. Bykova, J. Grafe, D. A. Bozhko, H. Y. Musiienko-Shmarova, V. Tiberkevich, A. N. Slavin, C. H. Back, J. Raabe, G. Schutz, and S. Wintz, Coherent Excitation of Heterosymmetric Spin Waves with Ultrashort Wavelengths, *Phys. Rev. Lett.* **122**, 117202 (2019).
- [48] K. An, V. S. Bhat, M. Mruczkiewicz, C. Dubs, and D. Grundler, Optimization of Spin-Wave Propagation with Enhanced Group Velocities by Exchange-Coupled Ferrimagnet-Ferromagnet Bilayers, *Phys. Rev. Applied* **11**, 034065 (2019).
- [49] R. Dreyer, N. Liebing, E. R. J. Edwards, A. Muller, and G. Woltersdorf, Spin-wave localization and guiding by magnon

- band structure engineering in yttrium iron garnet, *Phys. Rev. Materials* **5**, 064411 (2021).
- [50] J. Nogués, S. Stepanow, A. Bollero, J. Sort, B. Dieny, F. Nolting, and P. Gambardella, Simultaneous in-plane and out-of-plane exchange bias using a single antiferromagnetic layer resolved by x-ray magnetic circular dichroism, *Appl. Phys. Lett.* **95**, 152515 (2009).
- [51] A. Manchon, J. Železný, I. M. Miron, T. Jungwirth, J. Sinova, A. Thiaville, K. Garello, and P. Gambardella, Current-induced spin-orbit torques in ferromagnetic and antiferromagnetic systems, *Rev. Mod. Phys.* **91**, 035004 (2019).
- [52] X. Ma, G. Yu, S. A. Razavi, S. S. Sasaki, X. Li, K. Hao, S. H. Tolbert, K. L. Wang, and X. Li, Dzyaloshinskii-Moriya Interaction across an Antiferromagnet-Ferromagnet Interface, *Phys. Rev. Lett.* **119**, 027202 (2017).
- [53] H. Yu, R. Huber, T. Schwarze, F. Brandl, T. Rapp, P. Berberich, G. Duerr, and D. Grundler, High propagating velocity of spin waves and temperature dependent damping in a CoFeB thin film, *Appl. Phys. Lett.* **100**, 262412 (2012).
- [54] Y. Tserkovnyak, A. Brataas, and G. E. W. Bauer, Enhanced Gilbert Damping in Thin Ferromagnetic Films, *Phys. Rev. Lett.* **88**, 117601 (2002).
- [55] R. E. De Wames and T. Wolfram, Dipole-exchange spin waves in ferromagnetic films, *J. Appl. Phys.* **41**, 987 (1970).
- [56] B. A. Kalinikos and A. N. Slavin, Theory of dipole-exchange spin wave spectrum for ferromagnetic films with mixed exchange boundary conditions, *J. Phys. C: Solid State Phys.* **19**, 7013 (1986).
- [57] N. Zhu, H. Chang, A. Franson, T. Liu, X. Zhang, E. Johnston-Halperin, M. Wu, and H. X. Tang, Patterned growth of crystalline  $Y_3Fe_5O_{12}$  nanostructures with engineered magnetic shape anisotropy, *Appl. Phys. Lett.* **110**, 252401 (2017).
- [58] H. Yu, O. d'Allivy Kelly, V. Cros, R. Bernard, P. Bortolotti, A. Anane, F. Brandl, R. Huber, I. Stasinopoulos, and D. Grundler, Magnetic thin-film insulator with ultra-low spin wave damping for coherent nanomagnonics, *Sci. Rep.* **4**, 6848 (2014).
- [59] H. Qin, S. J. Hamalainen, K. Arjas, J. Witteveen, and S. van Dijken, Propagating spin waves in nanometer-thick yttrium iron garnet films: Dependence on wave vector, magnetic field strength, and angle, *Phys. Rev. B* **98**, 224422 (2018).
- [60] H. Wang, J. Chen, T. Liu, J. Zhang, K. Baumgaertl, C. Guo, Y. Li, C. Liu, P. Che, S. Tu, S. Liu, P. Gao, X. Han, D. Yu, M. Wu, D. Grundler, and H. Yu, Chiral Spin-Wave Velocities Induced by All-Garnet Interfacial Dzyaloshinskii-Moriya Interaction in Ultrathin Yttrium Iron Garnet Films, *Phys. Rev. Lett.* **124**, 027203 (2020).